Environ Fluid Mech (2013) 13:189–204
DOI 10.1007/s10652-012-9254-3

ORIGINAL ARTICLE

Turbulence and aeration in hydraulic jumps: free-surface fluctuation and integral turbulent scale measurements

Gangfu Zhang · Hang Wang · Hubert Chanson

Received: 24 May 2012 / Accepted: 4 September 2012 / Published online: 21 September 2012

Abstract In an open channel, a change from a supercritical to subcritical flow is a strong dissipative process called a hydraulic jump. Herein some new measurements of free-surface fluctuations of the impingement perimeter and integral turbulent time and length scales in the roller are presented with a focus on turbulence in hydraulic jumps with a marked roller. The observations highlighted the fluctuating nature of the impingement perimeter in terms of both longitudinal and transverse locations. The results showed further the close link between the production and detachment of large eddies in jump shear layer, and the longitudinal fluctuations of the jump toe. They highlighted the importance of the impingement perimeter as the origin of the developing shear layer and a source of vorticity. The air–water flow measurements emphasised the intense flow aeration. The turbulent velocity distributions presented a shape similar to a wall jet solution with a marked shear layer downstream of the impingement point. The integral turbulent length scale distributions exhibited a monotonic increase with increasing vertical elevation within $0.2 < L_z/d_1 < 0.8$ in the shear layer, where L_z is the integral turbulent length scale and d_1 the inflow depth, while the integral turbulent time scales were about two orders of magnitude smaller than the period of impingement position longitudinal oscillations.

Keywords Hydraulic jumps · Turbulence · Aeration · Free-surface fluctuations · Integral turbulent time scales · Integral turbulent length scales · Impingement perimeter · Jump toe · Physical measurements

1 Introduction

In an open channel, a hydraulic jump is the sudden and rapid transition from a supercritical to subcritical flow. The transition is an extremely turbulent flow associated with some turbulent energy dissipation, air entrainment, surface waves and spray, and it is characterised by strong

G. Zhang · H. Wang · H. Chanson (✉)
School of Civil Engineering, The University of Queensland, Brisbane, QLD 4072, Australia
e-mail: h.chanson@uq.edu.au
URL: http://www.uq.edu.au/~e2hchans/

Fig. 1 Photographs of prototype hydraulic jumps. **a** Hydraulic jump stilling basin in operation downstream of Paradise dam spillway (Australia) on 30 December 2010—Q = 6,300 m^3/s, Re = 1.9×10^7, **b** Hydraulic jump during Black Snake Creek flood, Marburg (QLD, Australia) on 11 Jan. 2011—flow from *foreground left* to *background left*, looking downstream

dissipative processes (Fig. 1). Figure 1a shows a hydraulic jump downstream of a dam spillway during a major flood, while Fig. 1b shows a smaller hydraulic jump during some inland flooding in South-East Queensland (Australia). In each case, the photographs highlight the intense turbulence and strong aeration in the natural flow. A hydraulic jump is characterised by a sudden rise in free-surface elevation (Figs. 1, 2). In an integral form, the continuity and momentum principles give a system of equations linking the flow properties upstream and downstream of the jump [9,16,19]. For a rectangular channel, it yields the classical Bélanger equation:

$$\frac{d_2}{d_1} = \frac{1}{2}\left(\sqrt{1 + 8\ \times Fr_1^2} - 1\right) \quad (1)$$

where d_2 and d_1 are respectively the downstream and upstream flow depths (Fig. 2), and Fr_1 is the inflow Froude number.

The turbulent flow in a hydraulic jump is extremely complicated, and it remains a challenge to scientists and researchers [5,8,15,22,27]. Some basic features of turbulent jumps include the turbulent flow motion with the development of large-scale vortices, the air bubble entrapment at the jump toe and the intense interactions between entrained air and coherent turbulent structures in the hydraulic jump roller, for example seen in Fig. 1. To date turbulence measurements in hydraulic jumps are limited, but for some pioneering works [29,30] and a few recent studies (Table 1). Table 1 regroups a number of recent physical studies in hydraulic jumps with a focus on the turbulent flow properties. Some studies aimed to characterised the

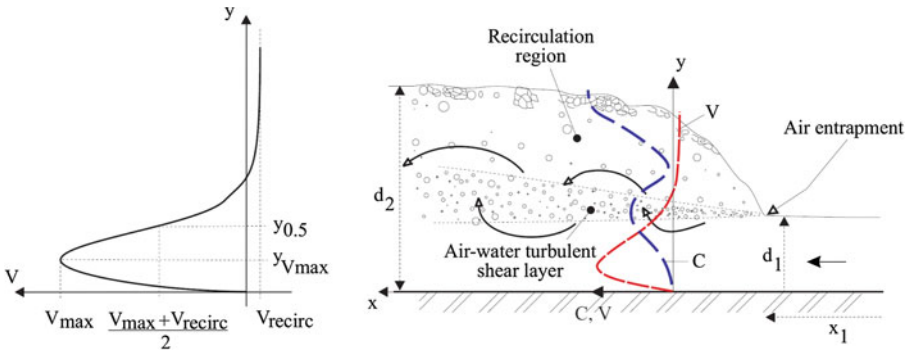

Fig. 2 Definition sketch of flow aeration at a hydraulic jump—details of velocity distribution in the roller

air–water turbulent flow properties [4,7,24], while other works focused on the free-surface fluctuating properties and the relationships between instantaneous free-surface fluctuations and air–water flow properties [3,25].

This paper presents some new physical experiments performed in a relatively large physical facility operating at large Reynolds numbers ($2.5 \times 10^4 < Re < 1.0 \times 10^5$) and covering a relatively wide range of inflow conditions ($2.6 < Fr_1 < 8.9$, $10 < x_1/d_1 < 60$). Such flow conditions would be representative of some small storm waterways during flood events and could be considered as a 10:1 to 20:1 scale study of the hydraulic jump seen in Fig. 1b. The focus is on the jump toe and its fluctuating shape, and the turbulence in the marked roller. The results emphasise the complicated nature of hydraulic jump flow motion and turbulence characteristics. Herein the aim of the study is a detailed characterisation of the turbulent flow properties in the developing shear layer supported by detailed air–water flow properties in the hydraulic jump flow.

2 Physical modelling and instrumentation

2.1 Presentation

The experimental study was performed in a down-scaled facility compared to the prototype hydraulic jumps seen in Fig. 1. For a hydraulic jump in a horizontal channel with rectangular cross section (Figs. 2, 3), the parameters involved in physical modelling include the fluid properties, the geometrical scales, the flow conditions, the two-phase flow properties of the jump, the time-dependent properties of the jump, and the fluid properties and physical constants [28,34]. The dimensional analysis may be simplified within some basic simplifications. Herein the compressibility of the two-phase flow was not taken into account, the air and water properties were related as functions of the local void fraction, and the temperature was considered to be constant. Lastly the flow may be assumed to be two-dimensional, although the present results might suggest that the approximation is gross. Consequently, a simplified dimensional analysis yields a series of relationships between the hydraulic jump flow properties and the initial and boundary conditions:

$$C, \frac{F \times d_1}{V_1}, \frac{V}{V_1}, \frac{u'}{V_1}, T_z \times \sqrt{\frac{g}{d_1}}, \frac{L_z}{d_1}, \frac{F_{toe} \times d_1}{V_1}, \frac{F_{vort} \times d_1}{V_1}, \ldots$$

Table 1 Experimental flow conditions of hydraulic jump studies

References	d_1 (m)	x_1 (m)	Fr_1	Re	Instrumentation	Remarks
(1)	(2)	(3)	(4)	(5)	(6)	(7)
Present study	0.025 to 0.027	0.25, 0.50, 1.0, 1.5	2.8 to 7.5	3.8×10^4 to 7.6×10^4	Video-camera	Series HW2011 W = 0.5 m
	0.024 to 0.028	1.0	2.6 to 8.9	3.6×10^4 to 1.0×10^5	Conductivity probes	Series GZ201011 W = 0.5 m
[4]	0.013 to 0.029	0.50 & 1.0	5.1 to 8.6	2.5×10^4 to 9.8×10^4	Conductivity probes	W = 0.25 & 0.5 m
[25]	0.018	0.75	5.1 to 8.3	3.8×10^4 to 6.2×10^4	Displacement meters Conductivity probe	W = 0.5 m
[7]	0.018	0.75	5.1 to 11.2	4.0×10^4 to 8.3×10^4	Video-camera Conductivity probe	W = 0.5 m
[3]	0.039 to 0.044	1.50	1.35 to 5.1	3.9×10^4 to 1.3×10^5	Displacement meters Conductivity probe	W = 0.5 m

d_1 inflow depth, Fr_1 inflow Froude number, *Re* Reynolds number, *W* channel width, x_1 upstream distance between the gate and jump toe

$$= f\left(\frac{W}{d_1}, \frac{x_1}{d_1}, \frac{\delta}{d_1}, \frac{x - x_1}{d_1}, \frac{y}{d_1}, Fr_1, Re, Mo, \ldots\right) \quad (2)$$

where C and F are the local void fraction and bubble count rate respectively, V and u' are the time-averaged interfacial velocity and turbulent velocity fluctuation respectively, d_1 and V_1 are the inflow depth and velocity (Fig. 2), T_z and L_z are respectively the integral turbulent time and length scales, F_{toe} and F_{vort} are the jump toe fluctuation frequency and vortex production rate respectively, W is the channel width, x is the longitudinal distance from the gate, x_1 is the jump toe position, δ is the boundary layer thickness in the inflow, y is the vertical distance, and Fr_1 and Re are respectively the inflow Froude number and Reynolds number defined as:

$$Fr_1 = \frac{V_1}{\sqrt{g \times d_1}} \quad (3)$$

$$Re = \frac{\rho \times V_1 \times d_1}{\mu} \quad (4)$$

with g the gravity constant, and ρ and μ the density and dynamic viscosity of water. The air–water surface tension σ is included in the Morton number $Mo = g \times \mu^4/(\rho \times \sigma^3)$ which is an invariant when the same fluids (air and water) are used in the experimental model as in prototype [6,26,34].

In practice, it is impossible to achieve the Froude and Reynolds similitude simultaneously with a geometrically similar model using the same fluids in model and prototype. The Froude similitude is typically selected because of theoretical considerations (Eq. (1)) [9,16,19]. This implies that the turbulence processes dominated by viscous forces might be affected by scale effects. Some scale effects in terms of void fraction, bubble count rate and bubble chord time distributions were highlighted in small size hydraulic jump models by [11] and [23]. Herein the experiments were performed with inflow Froude numbers ranging from 2.6 to 8.9 corresponding to Reynolds numbers between 3.6×10^4 to 1×10^5, most experiments being conducted with Reynolds numbers above the minimum value of 4×10^4 recommended by [23].

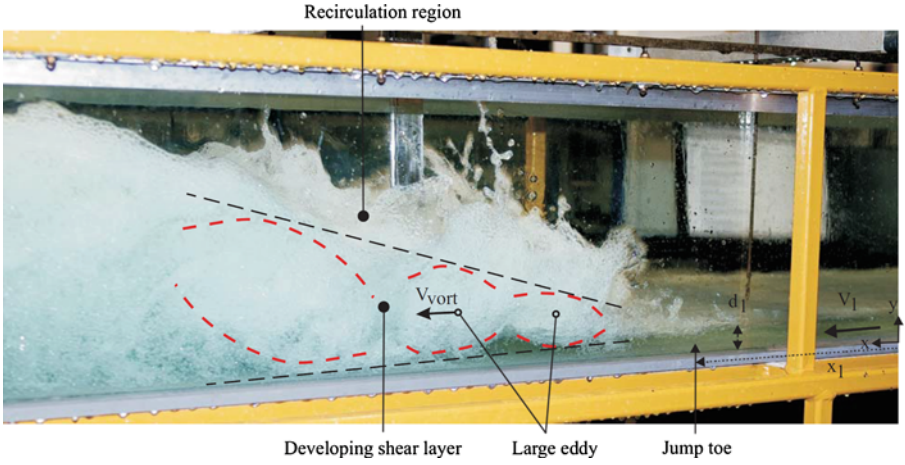

Fig. 3 Hydraulic jump experiment: *side view* with flow from *right* to *left*—flow conditions: $Fr_1 = 6.1$, $Re = 7 \times 10^4$

2.2 Physical facility and instrumentation

The physical experiments were performed in a smooth horizontal rectangular flume (Fig. 3). The 3.2 m long, 0.50 m wide channel had a PVC invert and glass sidewalls. The inflow conditions were controlled by a vertical gate equipped with a semi-circular rounding ($\varnothing = 0.3$ m). Its opening was fixed at $h = 0.024$ m for all experiments. The investigated flow conditions are summarised in Table 1.

The water discharge was measured with a Venturi meter calibrated on-site with an accuracy of $\pm 2\,\%$. The clear-water flow depths were measured using rail mounted pointer gauges with a 0.25 mm accuracy. The air–water flow properties were measured using a double-tip conductivity probes ($\varnothing = 0.25$ mm, $\Delta x = 7.1$ mm) and an array of two identical single-tip conductivity probe ($\varnothing = 0.35$ mm) separated by a known, controlled transverse distance Δz. An air bubble detector (UQ82.518) excited the probes and the output signals were scanned at 20 kHz per sensor for 45 s. The translation of the probes in the direction normal to the channel invert was controlled by a fine adjustment travelling mechanism connected to a Mitutoyo^{TM} digimatic scale unit. Flow visualisations were conducted with some high-shutter speed digital still- and video-cameras.

2.3 Signal processing

The operation principle of the phase detection needle probe was based upon the piercing of the air bubbles by the probe tip. Each detected air bubble would cause a drastic change in conductivity yielding a fast fluctuating, square-wave like probe signal (Fig. 4). Figure 4 presents a typical signal output of the double-tip probe.

The analysis of probe voltage outputs was based upon a single threshold technique set at 50 % of air–water voltage range for the void fraction, bubble count rate and bubble chord sizes. For example, the threshold level is shown in Fig. 4. A number of air–water flow properties were calculated, including the void fraction C, the bubble count rate F defined as the number of bubbles impacting the probe tip per second, and the air chord time distributions where the chord time is defined as the time spent by the bubble on the probe tip.

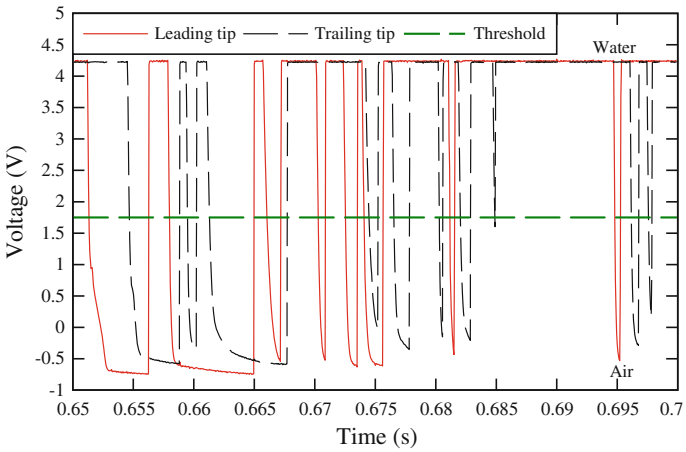

Fig. 4 Typical signal output of the double-tip probe in the bubbly flow region—flow conditions: $Fr_1 = 8.5$, $Re = 1.5 \times 10^4$, $d_1 = 0.024$ m, $x_1 = 0.83$ m, $y = 0.04$ m, $C = 0.174$, $F = 123$ Hz

The interfacial velocity V was calculated using a cross-correlation technique: $V = \Delta x/T$ where Δx is the longitudinal distance between both tips and T is the average interfacial travel time between probe sensors [13]. The turbulence level Tu was deduced from the shapes of cross- and auto-correlation functions [10,12]. The analysis of the signal auto-correlation function provided further information on the integral turbulent scales [4,10]. The integral turbulent length scale was calculated as

$$L_z = \int_{z=0}^{z=z((R_{xz})_{max}=0)} (R_{xz})_{max} \times dz \tag{5}$$

where z is the transverse (separation) distance and $(R_{xz})_{max}$ is the maximum normalised cross-correlation coefficient. The integral turbulent time scale was estimated as

$$T_z = \frac{1}{L_z} \times \int_{z=0}^{z=z((R_{xz})_{max}=0)} (R_{xz})_{max} \times T_{xz} \times dz \tag{6}$$

where T_{xz} is the integral cross-correlation time scale for a transverse separation distance dz.

3 General observations

3.1 Presentation

For inflow Froude numbers greater than 2 to 3, the hydraulic jump exhibited a marked roller associated a developing shear layer and large-scale vortical structures (Fig. 3). Figure 3 presents a typical side view of the breaking jump roller for $Fr_1 = 6.1$. At the impingement point or jump toe, a flow discontinuity developed and the impingement perimeter shape changed rapidly with time and transverse distance. Figure 5 illustrates some instantaneous

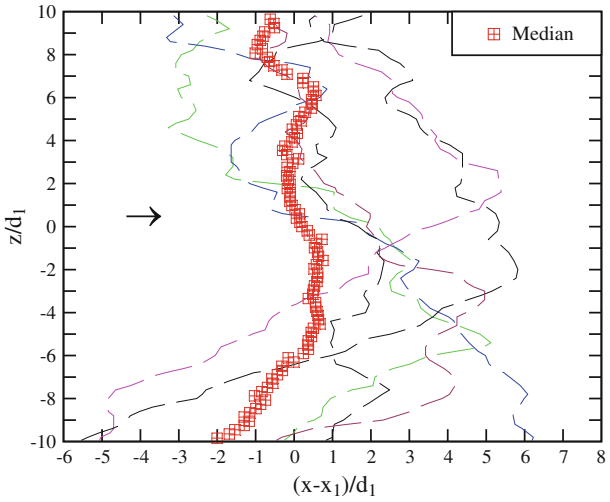

Fig. 5 Instantaneous hydraulic jump toe and median impingement perimeter transverse profiles in plan view—flow conditions: $Fr_1 = 6.0$, $x_1 = 0.5$ m (series HW2011)

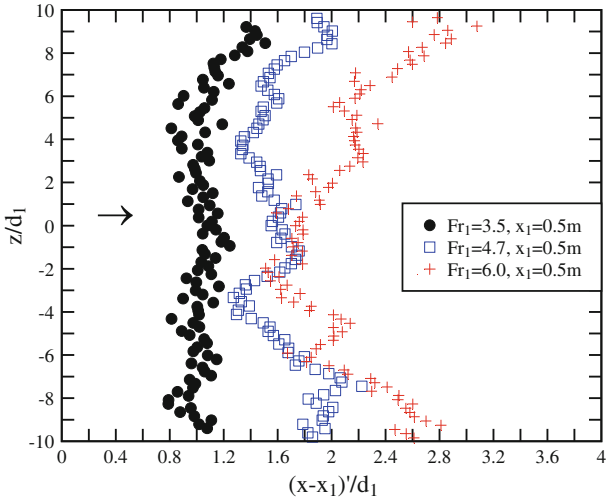

Fig. 6 Standard deviations of impingement perimeter profile ($x_1 = 0.5$ m, series HW2011)

impingement perimeter, viewed in elevation, together with the median profile. In Fig. 5, the arrow indicates the flow direction and each thin line represents an instantaneous impingement perimeter. Overall the perimeter data suggested the presence of transverse wave patterns with dimensionless wave length l_w/W between 2/3 and 2. The fluctuations in impingement perimeter transverse profile were significant and increased with increasing Froude number (Fig. 6). Figure 6 shows the transverse distributions of standard deviations of the impingement point location for three inflow Froude numbers, all experiments being performed with identical inflow depth d_1 and upstream distance from gate to jump toe x_1. The present observations implied that the approximation of two-dimensional flow might not be appropriate for any detailed study of the jump toe region.

The observations indicated that the average longitudinal position of the jump toe varied with time around a mean position x_1. The jump toe fluctuation frequency, the frequency of ejection of large vortical structures and the advection speed of these large coherent structures were investigated with video-cameras. Figure 3 illustrates a typical sideview picture. The hydraulic jump toe pulsations were believed to be caused by the growth, advection, and pairing of large-scale vortices in the developing shear layer [20]. The present observations showed indeed that the longitudinal oscillation frequency F_{toe} of the jump toe was close to the production rate F_{vort} of the large scale eddies in the shear layer. The physical results are presented in Fig. 7a, b. Within the experimental flow conditions, the data were best correlated by

$$\frac{F_{toe} \times d_1}{V_1} = 0.054 \times \exp(-0.33 \times Fr_1) \quad (7)$$

$$\frac{F_{vort} \times d_1}{V_1} = 0.034 \times \exp(-0.26 \times Fr_1) \quad (8)$$

irrespective of the jump toe location x_1. The present data are compared with Eqs. (7) and (8) as well as previous results in Fig. 7a, b. All the data were qualitatively in agreement and quantitatively of the same magnitude.

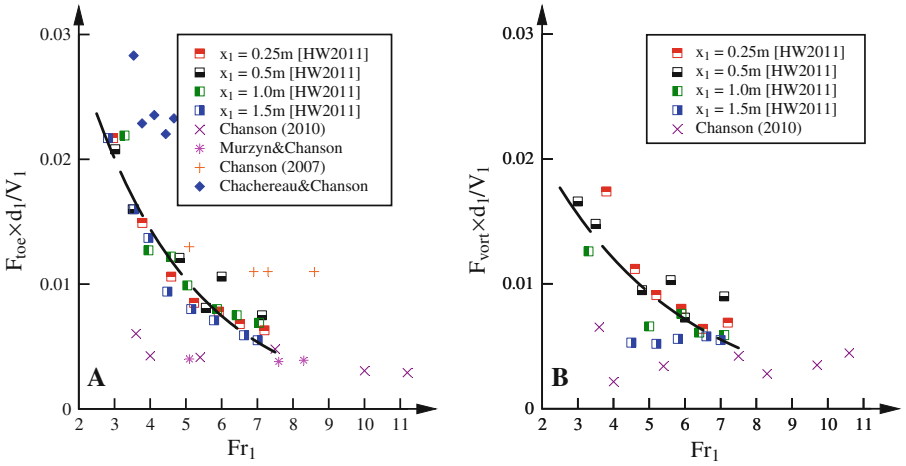

Fig. 7 Characteristic jump frequencies in terms of longitudinal jump toe fluctuation frequency and large vortical structure production rate—comparison with the earlier studies [3,4,7,25]. (**a**, *Left*) Dimensionless jump toe fluctuation frequency $F_{toe} \times V_1/d_1$, (**b**, *Right*) dimensionless frequency of large vortical structure production rate $F_{vort} \times V_1/d_1$

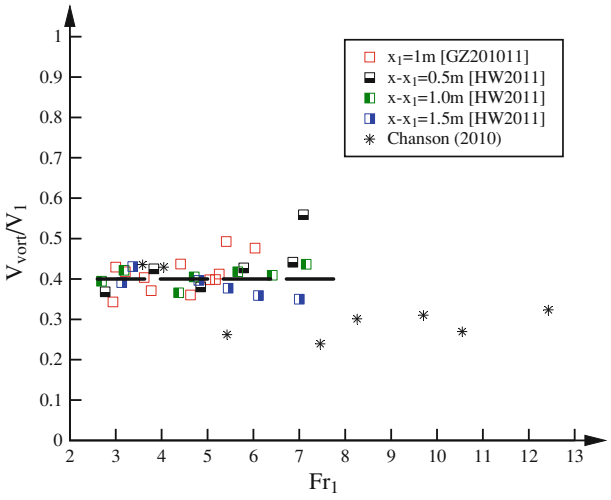

Fig. 8 Dimensionless advection speed V_{vort}/V_1 of large-scale vortical structures in the developing shear layer of hydraulic jumps—comparison with the data of [7]

The dimensionless advection speed V_{vort}/V_1 of large-scale coherent structures in the shear layer characterised the convection of large eddies in the mixing layer. The data were obtained from digital movie analyses and they are presented in Fig. 8 together with earlier findings. Overall the advection speed results were nearly independent of the inflow conditions and yielded on average (Fig. 8):

$$\frac{V_{vort}}{V_1} \approx 0.4 \tag{9}$$

The result (Eq. (9)) was obtained irrespective of the inflow Froude and Reynolds numbers, while the ratio of conjugate velocities V_2/V_1 ranged from 0.08 to 0.3.

4 Air–water turbulent flow properties

The measurements of void fraction and bubble count rate highlighted two dominant air–water flow regions. Namely, the air–water shear layer and the upper free-surface region (Fig. 3). The developing shear layer was characterised by some strong interactions between entrained air bubbles and vortical structures, associated with a local maximum in void fraction C_{max} and a maximum in bubble count rate F_{max}. In the shear layer, the distributions of void fractions followed an analytical solution of the advective diffusion equation for air bubbles:

$$C = \frac{\frac{Q_{air}}{Q}}{\sqrt{4\ \pi\ D^{\#}\ X'}} \times \left(\exp\left(-\frac{(y'-1)^2}{\frac{X'}{4 \times D^{\#}}} \right) + \exp\left(-\frac{(y'+1)^2}{\frac{X'}{4 \times D^{\#}}} \right) \right) \quad (10)$$

where Q_{air} is the entrained air volume, Q is the water discharge, $D^{\#}$ is a dimensionless air bubble diffusivity, $X' = X/d_1$, $y' = y/d_1$, $X = x\text{-}x_1 + u_r/V_1 \times y$, u_r is the bubble rise velocity [7]. In the upper free-surface region above, the void fraction increased monotically with increasing distance from the invert towards unity. Figure 9 presents some typical vertical distributions of void fraction and bubble count rate at different longitudinal locations along a hydraulic jump. In Fig. 9, the void fraction data were compared with Eq. (10). Figure 9 presents further some typical bubble count rate data. The results showed a peak value in the shear layer, with decreasing maximum bubble count rate F_{max} with increasing distance from the jump toe $(x - x_1)$ (Fig. 9). Importantly all the data shown in Fig. 9 were time-averaged measurements. [18] reported the simultaneous measurements of complete time series of vertical air concentration profiles highlighting the rapid fluctuations in instantaneous two-phase flow properties.

The interfacial velocity data showed some profiles with a self-similar shape close to wall jet results illustrated in Fig. 2 (Left). Namely, a flow region very close to the bed with a "boundary-layer like" profile where the velocity increases from zero up to a maximum velocity V_{max} at $y = Y_{V\,max}$, and an upper flow region with decreasing velocity with increasing vertical distance. The data showed distinctively the two regions (Fig. 10). Note that, in Fig. 10, there is no velocity data about $V \approx 0$ because the phase-detection dual-tip probe processing technique presents a singularity for zero velocity.

Overall the dimensionless velocity data were best fitted by a self-similar relationship:

$$\frac{V}{V_{max}} = \left(\frac{y}{Y_{V\,max}} \right)^{\frac{1}{N}} \quad \text{for } \frac{y}{Y_{V\,max}} < 1 \quad (11)$$

$$\frac{V - V_{recirc}}{V_{max} - V_{recirc}} = \exp\left(-\frac{1}{2} \times \left[1.765 \times \left(\frac{y - Y_{V\,max}}{y_{0.5}} \right) \right]^2 \right) \quad \text{for } 1 < \frac{y}{Y_{V\,max}} \quad (12)$$

where V_{recirc} is the recirculation velocity in the upper free-surface region with $V_{recirc} < 0$ typically, $y_{0.5}$ the vertical elevation where $V = V_{max}/2$ and N is a constant. The present results followed closely the above equations, despite some data scatter, as illustrated in Fig. 10 where the data are shown in a self-similar presentation. The finding was observed irrespective of the inflow Froude and Reynolds numbers within the investigated flow conditions (Table 1).

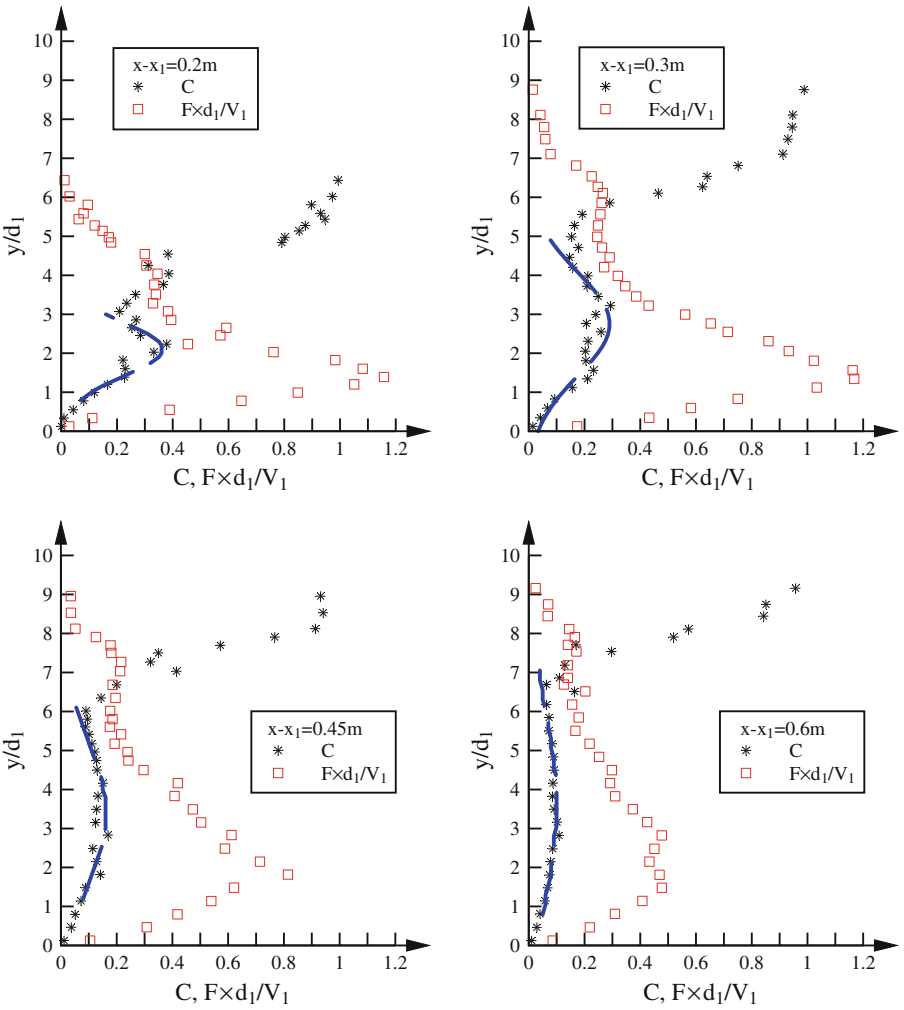

Fig. 9 Dimensionless distributions of void fraction and bubble count rate in hydraulic jump roller ($Fr_1 = 7.7$, $d_1 = 0.024$ m, $(x - x_1)/d_1 = 8.4, 12.6, 18.9\&25.2$, series GZ201011)—comparison between void fraction data and Eq. (10)

The maximum velocity data in the shear layer exhibited an exponential decay with increasing distance from the jump toe (Fig. 11). The data are presented in Fig. 11, in which they are compared with an empirical correction:

$$\frac{V_{max}}{V_1} = \exp\left(-\frac{1}{2} \times \frac{x - x_1}{d_1}\right) \tag{13}$$

first proposed by [7].

Based upon some detailed correlation analyses performed on the probe array signal outputs, the integral turbulent length and time scales, L_z and T_z respectively, were calculated. Typical results are presented in Figs. 12 and 13. The integral length scale L_z was closely linked with the sizes of large vortical structures. The present data indicated that $0.2 < L_z/d_1 < 0.8$

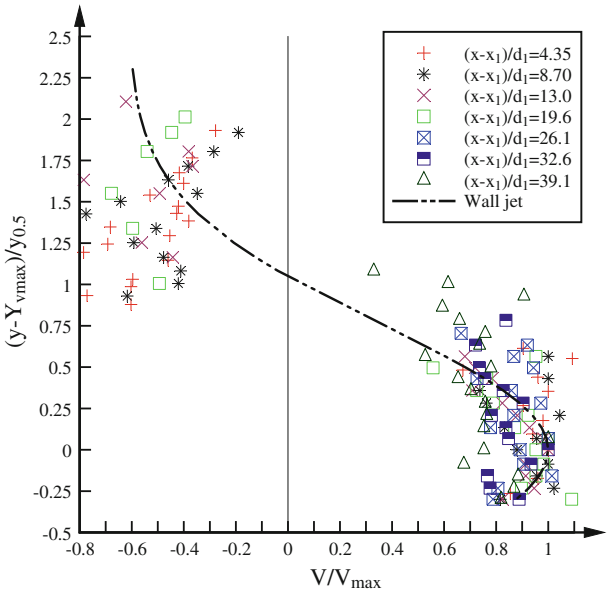

Fig. 10 Dimensionless velocity distributions V/V_{max} in hydraulic jumps: comparison between experimental data ($Fr_1 = 8.8$, $d_1 = 0.023$ m, $x_1 = 1$ m, series GZ201011) and Eq. (12)

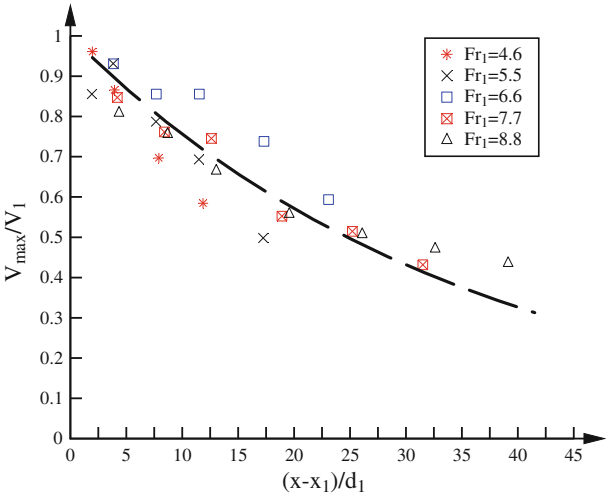

Fig. 11 Longitudinal variations of the dimensionless maximum velocity V_{max}/V_1 in the shear layer of hydraulic jumps (series GZ2011)—comparison with Eq. (13)

for a large majority of data independently of Froude number. For $y/d_1 < 4$, the turbulent length scale data presented a monotonic increase with increasing distance from the invert (Fig. 12). The data were best correlated by

$$\frac{L_z}{d_1} = \frac{0.6422}{\left(\frac{x-x_1}{d_1}\right)^{0.2411}} \times \left(\frac{y}{d_1}\right)^{0.8624/\sqrt{(x-x_1)/d_1}} \quad \text{for } \frac{y}{d_1} < 4 \tag{14}$$

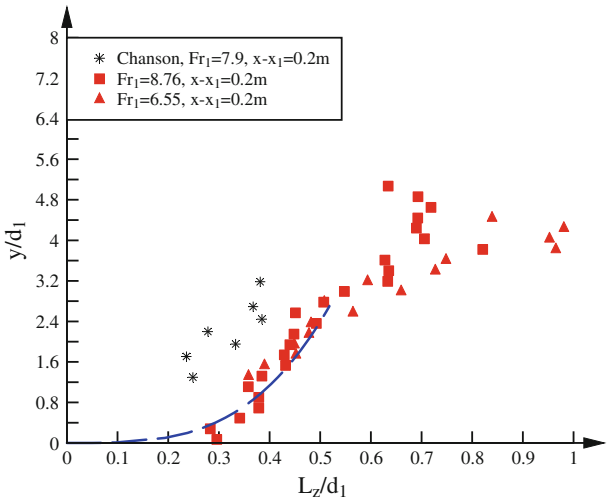

Fig. 12 Dimensionless distributions of integral turbulent length scale L_z/d_1 in hydraulic jumps at $x - x_1 = 0.2$ m: comparison between present data (series GZ201011), Chanson's data [4] and Eq. (14)

Basically the present results highlighted a self-similar vertical profile (Eq. (14)) of the integral turbulent length scale independently of the inflow Froude and Reynolds numbers.

The integral turbulent time scale T_z was linked with the life span of large eddies. The distributions of integral turbulent time scales (Fig. 13) showed a decrease with increasing distance from the invert. The results were within $1.7 < T_z \times (g/d_1)^{0.5} < 4$. Note that, in Fig. 13, top left graph, the data were collected very close to the jump toe ($x - x_1 = 0.1$ m). Measurements at that location were difficult because of the fluctuating nature of the jump toe location, and the data sampled at locations $y/d_1 > 2$ might be occasionally above the roller free-surface.

4.1 Discussion

A number of studies focused on the fundamentals of free-surface deformations and air–water free-surfaces: e.g., [1–3,21,25,31]. On the other hand, few results were reported to date in terms of the characteristic time and length scales in bubbly shear flows, but by [4] in hydraulic jumps and [14] in a stepped chute.

In the hydraulic jump roller, the characteristic length scale L_z is closely linked with the sizes of the large eddies and their vortex shedding (Fig. 3) [17]. Simply the integral length scale L_z characterises the transverse size of the large vortical structures advecting the bubbles. The present results highlighted that the transverse air–water length scales were indeed closely linked to the upstream flow depth: i.e., $L_z/d_1 = 0.2$ to 0.8 independently of the longitudinal distance and inflow Froude number (Fig. 12). For comparison, the size of the large eddies seen in Fig. 3 increased with increasing distance from the jump toe: e.g., their typical size increased from $2 \times d_1$ to $7 \times d_1$ from right to left (Fig. 3).

The integral time scale T_z is linked with the lifetime of the turbulent vortices with characteristic size L_z. The present findings showed some distinct differences between the production rate ($1/F_{vort}$) of large structures in the shear layer and the characteristic time scale T_z of the turbulent eddies That is, the integral time scale was about two orders of magnitude smaller

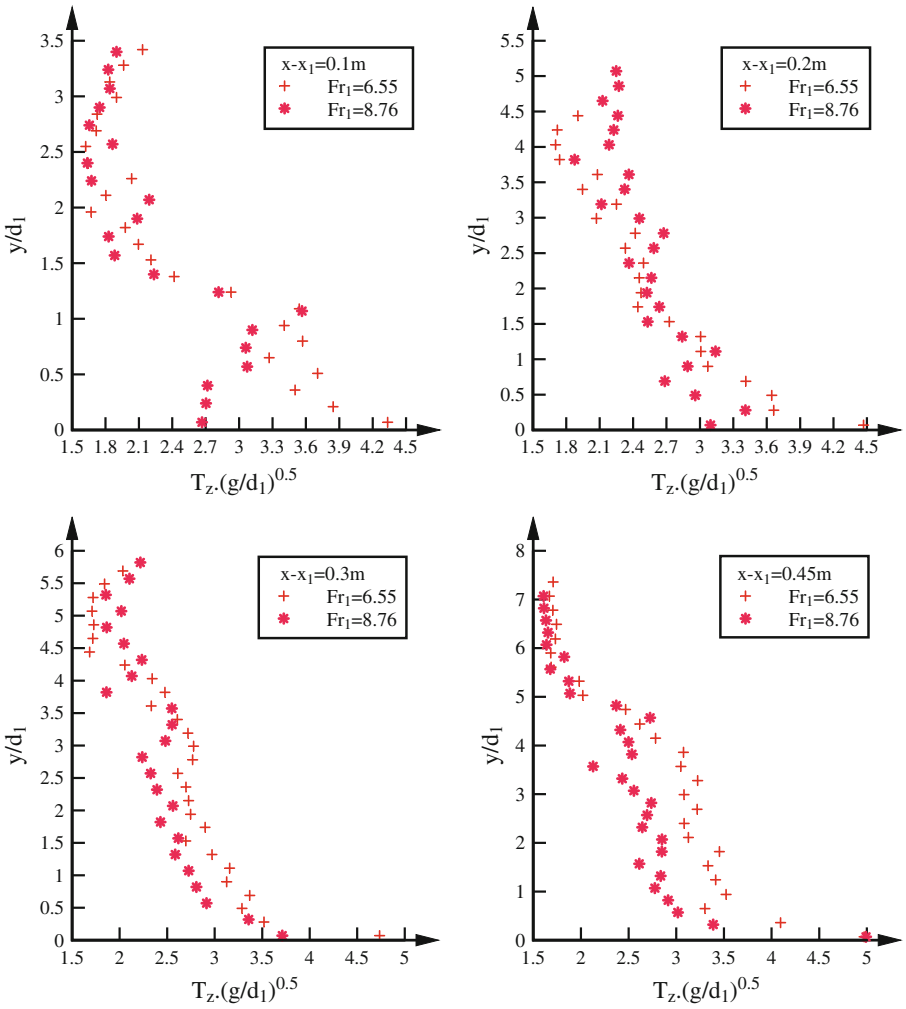

Fig. 13 Dimensionless distributions of integral turbulent length scale T_z/d_1 in hydraulic jumps—flow conditions: $Fr_1 = 6.5$ & 8.8, $(x - x_1)/d_1 = 8.4$, 12.6, 18.9 & 25.2, series GZ201011

than the characteristic period of the large eddy production rate with $1/(T_z \times F_{vort}) \approx 200$ to 300. The apparent discrepancy might be linked with the nature of the turbulent flow unsteadiness. The production of large eddies and the longitudinal oscillation of the jump toe induced a pseudo-periodic motion, such that the instantaneous velocity field combined three parts: a time-average, an organised oscillation component and a pseudo-random fluctuation. The non linear contribution of the organised fluctuations was shown to derive from coupled terms in the equations of motion [32,33]. It is hypothesised that the interactions between the pseudo-periodic motion, the high-frequency turbulent fluctuations and the entrained air bubble might cause some complex flow features.

Lastly the vertical distributions of both integral turbulent length and time scales exhibited a sharp break in shape, for example for $y/d_1 = 4$ at $(x - x_1)/d_1 = 8$. It is believed that this drastic change in distribution reflected the boundary between the air–water shear layer and the recirculation region above.

5 Conclusion

Detailed physical measurements were conducted in hydraulic jumps with Froude numbers between 2.6 and 8.9, inflow length x_1/d_1 between 10 and 60, and Reynolds numbers up to 1×10^5. The focus of the study was on the impingement perimeter properties and on the integral turbulent scales in the hydraulic jump roller.

The results highlighted the fluctuating nature of the impingement point in terms of both longitudinal and transverse directions. The transverse profile of the impingement perimeter varied rapidly in shape with time although its median position was about a straight line. The fluctuations of its transverse distributions increased with increasing Froude number. The perimeter data suggested the presence of transverse wave patterns, and the present observations implied that the approximation of two-dimensional flow would be inappropriate for any detailed study of the impingement point region. The production frequency F_{vort} of large coherent structures was very close to the jump toe longitudinal fluctuation frequency F_{toe}. The findings emphasised the close link between the production and detachment of large eddies in jump shear layer, and the longitudinal fluctuations of the jump toe. They highlighted further the importance of the impingement perimeter as the origin of the developing shear layer and a source of vorticity. The air–water flow properties showed the intense aeration of the roller with two dominant flow regions: that is, a developing shear layer and a recirculation region above. The turbulent velocity distributions presented a shape similar to a wall jet solution. The integral turbulent length scale data exhibited a monotonic increase with increasing vertical elevation within $0.2 < L_z/d_1 < 0.8$ in the shear layer, while the integral turbulent time scale was about two orders of magnitude smaller than the characteristic period of the production rate of large vortices in the shear layer.

The modelling of the air–water shear zone in turbulent hydraulic jumps remains naive because of the large number of relevant equations to describe the two-phase turbulent flow motion as well as the limited validation data sets. To date the most successful physical data set were obtained with intrusive phase-detection probes including this study. A future research direction in hydraulic jump study may see the development of composite models embedding numerical and physical studies.

Acknowledgments The authors thank Ahmed Ibrahim and Jason Van Der Gevel (The University of Queensland) for the technical assistance. The financial support of the Australian Research Council (Grants DPDP0878922 & DP120100481) is acknowledged.

References

1. Brocchini M, Peregrine DH (2001) The dynamics of strong turbulence at free surfaces. Part 1. Description. J Fluid Mech 449:225–254
2. Brocchini M, Peregrine DH (2001) The dynamics of strong turbulence at free surfaces. Part 2. Free-surface boundary conditions. J Fluid Mech 449:255–290
3. Chachereau Y, Chanson H (2011) Free-surface fluctuations and turbulence in hydraulic jumps. Exp Thermal Fluid Sci 35(6):896–909. doi:10.1016/j.expthermflusci.2011.01.009
4. Chanson H (2007) Bubbly flow structure in hydraulic jump. Eur J Mech B 26(3):367–384. doi:10.1016/j.euromechflu.2006.08.001
5. Chanson H (2009) Current knowledge in hydraulic jumps and related phenomena. A survey of experimental results. Eur J Mech B 28(2):191–210. doi:10.1016/j.euromechflu.2008.06.004
6. Chanson H (2009) Turbulent air–water flows in hydraulic structures: dynamic similarity and scale effects. Environ Fluid Mech 9(2):125–142. doi:10.1007/s10652-008-9078-3
7. Chanson H (2010) Convective transport of air bubbles in strong hydraulic jumps. Int J Multiph Flow 36(10):798–814. doi:10.1016/j.ijmultiphaseflow.2010.05.006

8. Chanson H (2011) Hydraulic jumps: turbulence and air bubble entrainment. Journal La Houille Blanche 1:5–16 & Front cover. doi:10.1051/lhb/2011026 (ISSN 0018-6368)
9. Chanson H (2012) Momentum considerations in hydraulic jumps and bores. J Irrigation Drainage Eng ASCE 138(4):382–385. doi:10.1061/(ASCE)IR.1943-4774.0000409
10. Chanson H, Carosi G (2007) Advanced post-processing and correlation analyses in high-velocity air–water flows. Environ Fluid Mech 7(6):495–508. doi:10.1007/s10652-007-9038-3
11. Chanson H, Gualtieri C (2008) Similitude and scale effects of air entrainment in hydraulic jumps. J Hydraul Res IAHR 46(1):35–44
12. Chanson H, Toombes L (2002) Air–water flows down stepped chutes: turbulence and flow structure observations. Int J Multiph Flow 27(11):1737–1761
13. Crowe C, Sommerfield M, Tsuji Y (1998) Multiphase flows with droplets and particles. CRC Press, Boca Raton
14. Felder S, Chanson H (2009) Turbulence, dynamic similarity and scale effects in high-velocity free-surface flows above a stepped chute. Exp Fluids 47(1):1–18. doi:10.1007/s00348-009-0628-3
15. Hager WH (1992) Energy dissipators and hydraulic jump. Kluwer Academic Publ, Water Science and Technology Library 8, Dordrecht, The Netherlands
16. Henderson FM (1966) Open channel flow. MacMillan Company, New York, USA
17. Hoyt JW, Sellin RHJ (1989) Hydraulic jump as 'mixing layer'. J Hydraul Eng ASCE 115(12):1607–1614
18. Leandro J, Carvalho R, Chachereau Y, Chanson H (2012) Estimating void fraction in a hydraulic jump by measurements of pixel intensity. Exp Fluids 52(5):1307–1318. doi:10.1007/s00348-011-1257-1
19. Liggett JA (1994) Fluid mechanics. McGraw-Hill, New York
20. Long D, Rajaratnam N, Steffler PM, Smy PR (1991) Structure of flow in hydraulic jumps. J Hydraul Res IAHR 29(2):207–218
21. Mouaze D, Murzyn F, Chaplin JR (2005) Free surface length scale estimation in hydraulic jumps. J Fluids Eng Trans ASME 127:1191–1193
22. Murzyn F (2010) Assessment of different experimental techniques to investigate the hydraulic jump: do they lead to the same results? In: Janssen R, Chanson H (eds) Hydraulic structures: useful water harvesting systems or relics? Proceedings of the 3rd international junior researcher and engineer workshop on hydraulic structures (IJREWHS'10), 2–3 May 2010, Edinburgh, Scotland. Hydraulic Model Report CH80/10, School of Civil Engineering, The University of Queensland, Brisbane, Australia, pp 3–36
23. Murzyn F, Chanson H (2008) Experimental assessment of scale effects affecting two-phase flow properties in hydraulic jumps. Exp Fluids 45(3):513–521. doi:10.1007/s00348-008-0494-4
24. Murzyn F, Chanson H (2009) Experimental investigation of bubbly flow and turbulence in hydraulic jumps. Environ Fluid Mech 9(2):143–159. doi:10.1007/s10652-008-9077-4
25. Murzyn F, Chanson H (2009) Free-surface fluctuations in hydraulic jumps: experimental observations. Exp Thermal Fluid Sci 33(7):1055–1064. doi:10.1016/j.expthermflusci.2009.06.003
26. Pfister M, Chanson H (2012) Scale effects in physical hydraulic engineering models. Discussion. J Hydraul Res IAHR 50(2):244–246. doi:10.1080/00221686.2012.654672
27. Rajaratnam N (1967) Hydraulic jumps. In: Chow VT (ed) Advances in hydroscience, vol 4. Academic Press, New York, pp 197–280
28. Rao NSL, Kobus HE (1971) Characteristics of self-aerated free-surface flows. Water and waste water/current research and practice 10. Eric Schmidt, Berlin
29. Resch FJ, Leutheusser HJ (1972) Le Ressaut Hydraulique: Mesure de Turbulence dans la Région Diphasique (The hydraulic jump: turbulence measurements in the two-phase flow region) Jl La Houille Blanche 4:279–293 (in French)
30. Rouse H, Siao TT, Nagaratnam S (1959) Turbulence characteristics of the hydraulic jump. Trans ASCE 124:926–950
31. Sarpkaya T (1996) Vorticity, free surface and surfactants. Ann Rev Fluid Mech 28:83–128
32. Schlichting H, Gersten K (2001) Boundary layer theory, 8th ed. Springer, Berlin
33. Telionis DP (1981) Unsteady viscous flows. Springer, Springer Series in Computational Physics, Berlin
34. Wood IR (1991) Air entrainment in free-surface flows. IAHR hydraulic structures design manual no. 4, hydraulic design considerations. Balkema Publ, Rotterdam